Video Article

Synchrotron X-ray Microdiffraction and Fluorescence Imaging of Mineral and Rock Samples

Camelia V. Stan[1], Nobumichi Tamura[1]

[1]Advanced Light Source, Lawrence Berkeley National Laboratory

Correspondence to: Nobumichi Tamura at ntamura@lbl.gov

URL: https://www.jove.com/video/57874
DOI: doi:10.3791/57874

Keywords: Engineering, Issue 136, Laue diffraction, diffraction, x-rays, mapping, synchrotron, mineralogy, petrology, single crystal, semiconductor, x-ray microbeam, microdiffraction, microfluorescence

Date Published: 6/19/2018

Citation: Stan, C.V., Tamura, N. Synchrotron X-ray Microdiffraction and Fluorescence Imaging of Mineral and Rock Samples. *J. Vis. Exp.* (136), e57874, doi:10.3791/57874 (2018).

Abstract

In this report, we describe a detailed procedure for acquiring and processing x-ray microfluorescence (µXRF), and Laue and powder microdiffraction two-dimensional (2D) maps at beamline 12.3.2 of the Advanced Light Source (ALS), Lawrence Berkeley National Laboratory. Measurements can be performed on any sample that is less than 10 cm x 10 cm x 5 cm, with a flat exposed surface. The experimental geometry is calibrated using standard materials (elemental standards for XRF, and crystalline samples such as Si, quartz, or Al_2O_3 for diffraction). Samples are aligned to the focal point of the x-ray microbeam, and raster scans are performed, where each pixel of a map corresponds to one measurement, *e.g.,* one XRF spectrum or one diffraction pattern. The data are then processed using the in-house developed software XMAS, which outputs text files, where each row corresponds to a pixel position. Representative data from moissanite and an olive snail shell are presented to demonstrate data quality, collection, and analysis strategies.

Video Link

The video component of this article can be found at https://www.jove.com/video/57874/

Introduction

Crystalline samples frequently display heterogeneity on the micron scale. In geoscience, the identification of minerals, their crystal structure, and their phase relations in 2D systems is important for understanding both the physics and chemistry of a particular system, and requires a spatially-resolved, quantitative technique. For example, relationships between minerals can be examined based on the phase distribution within a localized 2D region. This can have implications for the history and chemical interaction that may have occurred within a rocky body. Alternatively, the material structure of a single mineral can be examined; this may determine the types of deformation that the mineral may have been or is currently being subjected to (such as in the case of an *in situ* deformation experiment with a device like the diamond anvil cell). In geoscience, these analyses are often performed using a combination of scanning electron microscopy (SEM) with energy or wavelength dispersive x-ray spectroscopy (E/WDS) and electron backscatter diffraction (EBSD). However, sample preparation can be difficult, involving extensive polishing and mounting for vacuum measurements. Also, EBSD is a surface technique that requires relatively unstrained crystals, which is not always the case for geological materials which may have experienced uplift, erosion, or compression.

Spatially-resolved characterization using 2D x-ray microdiffraction and XRF mapping, as is available at beamline 12.3.2 of the ALS, is a fast and straightforward way of making large area maps of single or multiphase systems where the crystal size is on the scale of a few nanometers (in the case of polycrystalline samples) to hundreds of microns. This method has many advantages when compared to other commonly used techniques. Unlike other 2D crystal mapping techniques, such as EBSD, microdiffraction samples can be measured at ambient conditions, and thus do not require special preparation as there is no vacuum chamber. Microdiffraction is suitable for crystals that are pristine as well as those which have experienced severe strain or plastic deformation. Samples such as thin sections are commonly examined, as are materials embedded in epoxy, or even unaltered rocks or grains. Data collection is fast, usually less than 0.5 s/pixel for Laue diffraction, less than 1 min/pixel for powder diffraction, and less than 0.1 s/pixel for XRF. Data are stored locally, temporarily on a local storage, and more permanently at the National Energy Research Scientific Computing (NERSC) center, from which it is easy to download. Data processing for diffraction can be performed on a local cluster or on a NERSC cluster in under 20 min. This allows for fast throughput in data collection and analysis, and for large area measurements over a short period of time when compared to laboratory instruments.

This method has a wide variety of applications and has been used extensively, particularly in materials science and engineering, to analyze everything from 3D-printed metals[1,2], to solar panel deformation[3], to strain in topological materials[4], to memory alloy phase transitions[5], to the high-pressure behavior of nanocrystalline materials[6,7]. Recent geoscience projects include the analysis of strain in various quartz samples[8,9] of volcanic cementitious processes[10,11], and also of biominerals such as calcite and aragonite in shells and corals[12,13] or apatite in teeth[14], and additional studies on meteorite phase distribution, mineral structure identification of new minerals, and plastic deformation response in high-pressure silica have also been collected. The techniques used at beamline 12.3.2 are applicable to a broad range of samples, relevant to anyone in the mineralogical or petrological communities. Here we outline the data acquisition and analysis protocol for beamline 12.3.2, and present several applications in order to demonstrate the usefulness of the combined XRF and Laue/powder microdiffraction technique in the geoscience field.

Before going into experimental detail, it is germane to discuss the setup of the end-station (see **Figure 1** and **Figure 4** in Kunz *et al.*[15]). The x-ray beam exits the storage ring and is directed using a toroidal mirror (M201), the purpose of which is to refocus the source at the entrance of the experimental hutch. It passes through a set of roll slits which function as a secondary source point. It is then monochromatized (or not) depending on the experiment type, before passing through a second set of slits and being focused to micron sizes by a set of Kirkpatrick-Baez (KB) mirrors. The beam then passes through an ion chamber, whose signal is used to determine beam intensity. Attached to the ion chamber is a pinhole, which blocks scattered signal from impinging onto the detector. The focused beam then encounters the sample. The sample is placed on top of a stage, which consists of 8 motors: one set of rough (lower) x, y, z motors, one set of fine (upper) x, y, z motors, and two rotation motors (Φ and χ). It can be visualized with three optical cameras: one with low zoom, placed at the top of the ion chamber, one with high zoom, placed in a plane at an approximately 45° angle with respect to the x-ray beam, and a second high-zoom camera placed at a 90° angle with respect to the x-ray beam. This last one works best for samples that are oriented vertically (such as for a transmission mode experiment), and imaging is performed using a wedge-shaped mirror attached to the pinhole. The x-ray diffraction detector is located on a large rotating stage, and both the angle and the vertical displacement of the detector can be controlled. A silicon drift detector to collect XRF is also present. Samples can be prepared in any manner, as long as the exposed region of interest (ROI) is flat (on the micron scale) and uncovered or covered in no more than ~50-100 µm of x-ray transparent material such as polyimide tape.

The procedure outlined below describes an experiment that takes place in reflective geometry, and assumes the z direction is normal to the sample and x and y are the horizontal and vertical scanning directions, respectively. Because of the flexibility of the stage and detector system, however, some experiments are performed in transmission geometry, where the x and z directions are the horizontal and vertical scanning directions, while y is parallel to the direct beam (see Jackson *et al.*[10,11]).

Protocol

1. Set Up Beamline and Collect Data

NOTE: Calibration standards and samples are collected in the same manner, with the main difference lying in the processing method.

1. **Mount the sample and close the experimental hutch.**
    1. Attach a sample to the top half of a kinematic base (see **Table of Materials**) such that the ROI is vertically displaced relative to the base by at least 15 mm.
    NOTE: A standard block exists at the beamline for use with samples < 20 mm thick. The bottom half of the kinematic base is permanently installed on the stage system of the beamline.
    2. Place the sample and base on top of the stage inside of the experimental hutch. Close the experimental hutch.

2. **Turn on the beamline control and data acquisition software.**
    1. Open the beamline control program. Click the arrow in the upper left-hand corner to initialize the program. Wait for all signal lights on the right-hand side to turn green, indicating that the software has initialized.
    2. Click on any beamline component to initialize the control panel for that component. This applies primarily to the translation stage, and to the slit controls.
    3. Initialize the x-ray diffraction scan software from the desktop.
    NOTE: This must be done only after the beamline control program has completely turned on, otherwise the programs cannot communicate correctly, and the mapping procedure will not work.

3. **Bring the sample into the focal point of the x-ray beam.**
    1. Turn on the alignment laser by clicking on the button labeled "laser".
    2. Translate the upper x, y, and z stages by using the stage alignment menu and clicking on the up and down arrows to bring the ROI of the sample within approximate visual focus of the rough alignment camera. Adjust the distance that each motor can be jogged by typing in the desired value.
    NOTE: The stages are motorized and controlled with the beamline software.
    3. While looking at the fine-focus camera, translate the upper z motor until the laser spot is aligned with the mark on the screen.
    NOTE: If this maneuver is performed consistently for each sample, all sample-to-detector parameters will remain the same.

4. **Select either the white (polychromatic) light or monochromatic mode.**
    1. Roll slits at the entrance of the experimental hutch to define the final focus demagnification and thus beam size on the sample.Note: They function as a source point for the x-rays, prior to focusing by a set of KB mirrors located downstream of the monochromator. Roll slit size can be increased to increase flux (for instance in monochromatic mode) at the expense of increased beam size on sample.
    2. Ensure that the correct roll slits setting is used: 8 µm x 16 µm for white beam applications or 100 µm x 100 µm for monochromatic applications.
    3. For experiments performed in monochromatic mode, move the monochromator to the desired energy by typing in an energy between 6,000 and 22,000 eV before increasing the roll slit size.

5. **Tune the beam intensity using the pre-focusing M201 mirror.**
    1. Open the control menu by going to **Motors | Display**. Select **M201 pitch** from the list of motors. Jog in 5 count increments until the ion chamber (IC) count value is maximized.
    2. The motor has a long backlash, so perform this procedure slowly.

6. **Map the sample using XRF.**

    1. Initialize fluorescence mapping from the **Scans | XRF Scanning** menu. Change the file name and folder location for the XRF measurement to the correct designations.
    2. Add up to 8 elements of interest, by typing in a range of energies between 2-20 keV that encompasses one of the main emission lines of a particular element.
    NOTE: If the system is operating in monochromatic mode, the elemental energy range must be at least ~1 keV below the monochromatic energy used to generate the fluorescence line in order to induce the fluorescence process (see Beckhoff *et al.*[16]).
    3. Using the upper x and y motors, define a rectangular area where mapping will take place by using the stage software to drive to two opposing corners. Set them as the start and end positions by clicking on **Set to Current Pos** in the setup menu.
    NOTE: The map can be of any size within the travel limit of the stages.
    4. Enter either the velocity or the dwell time for the scan. Verify that the map covers the ROI for the sample by pressing the **To Start** and **To End** buttons to see the diagonally opposite corners that have been selected to define the map.
    5. Start the scan by clicking the **Start** button. At this point, the measurement will proceed until all points have been scanned.
    NOTE: The program will save a text file of values, where each row corresponds with a motor position and each column corresponds to a readout such as motor, total incoming beam intensity, measured element intensity, *etc.* These can then be replotted in any graphing program. The measurement program also displays element maps in real time.

7. **Map the sample using x-ray diffraction.**
    1. Type in a username in the x-ray diffraction scan window for the data collection process to generate the main folder within which all data will be written.
    2. Type in a sample name.
    NOTE: All diffraction patterns for the sample will be in a folder of this name, and they will be labeled sample_name_xxxxx.tif, where xxxxx is a string of numbers, typically starting from 00001.
    3. Ensure that "Upper X" and "Upper Y" are selected as the x and y scanning motors. The system is designed to scan over many of the available beamline motors, depending on the type of experiment being performed. For most scenarios, scans will be performed in either xy, xz, or in monochromatic energy (to map single crystal peak positions; this is a 1D scan).
    4. Type in x and y start and end positions for the map.
    5. Type in x and y step sizes, and pattern exposure time.
    NOTE: Single crystal scans using the full white beam proceed faster because the beam flux is orders of magnitude greater than that of a monochromatic scan. Consequently, single crystal pattern exposures tend to be < 1 s, whereas monochromatic scan exposures (such as for powder diffraction) tend to be > 10 s. After the step size and exposure time are entered, the program will estimate the total scan time required for the entire map to be collected.
    6. Click the play button to launch mapping.
    NOTE: The program will now automatically move to a specified motor position/map pixel and record a diffraction pattern, then progress through each pixel until the map is completely recorded as a sequence of .tif files.

2. Process Data Using the Beamline-developed X-ray Microdiffraction Analysis Software (XMAS)[17]

1. **Load patterns**
    1. Open XMAS[17]. Load a diffraction pattern by going to **File | Load Image** and selecting a pattern. Subtract the detector background by going to **Image | Fit and Remove Background**.
    2. Load a calibration file by going to **Parameters | Calibration Parameters**. Click on **Load Calib** and select the appropriate calibration parameter file.
    NOTE: The calibration parameter file will contain information such as the pixel size ratio (which is always fixed), detector distance (between the focal point on the sample and the detector center), detector angular position, xcent (center of the detector in x), ycent (center of the detector in y), pitch, yaw, and roll of the detector, sample orientation, as well as wavelength if using monochromatic light.

2. **Process single crystal data.**
    1. Index patterns
        1. Load a standard crystal structure file (.cri) by going to **Parameters | Crystal Structure** and selecting the appropriate file. If stress values must be calculated, load a stiffness file (.stf), containing the third order elastic tensor matrix for the material.
        NOTE: The .cri file would contain the space group number, all six lattice parameters, the number of Wyckoff atomic positions and atom types, fractional coordinates, and occupancies.
        2. To calculate the crystal grain orientation, go to **Parameters | Crystal Orientation parameters for Laue**. Type in "hkl plane normal" for in plane and out of plane orientation.
        3. Find sample peaks by going to **Analysis | Peak Search**.
            1. Select a peak threshold (*e.g.,* signal/noise ratio) to a value between 5 and 50, depending on the intensity of the diffraction pattern.
            2. Click the **Go!** button to initiate the peak search. Add any peaks not picked by the program, and remove any dead peaks.

        4. Initialize indexing by going to **Analysis | Laue Indexing**.

    2. Determine the strain and/or stress.
        1. If stress does not need to be quantified, skip this step. Otherwise, go to **Parameters | Crystal structure** and load the stiffness file (.stf) associated with the crystal structure.
        NOTE: The file consists of the third-order stiffness tensor matrix for the particular material. Examples are provided with the XMAS software.
        2. Select stress parameters.

        1. Go to **Parameters | Strain/Calibration Laue refinement parameters**. A new window will open, with calibration parameters for the experimental system on the right side and strain refinement parameters on the left side.
        2. Select appropriate strain refinement parameters for the sample.
        3. Make sure the **refine orientation** box is also selected, if refinement of the crystal orientation is desired.

    3. Initialize strain calculation by going to **Analysis | Strain Refinement/Calibration**.

3. Calculate and display the 2D maps.
    1. Open the analysis procedure from **Automated Analysis | Set automatic analysis of Laue Patterns**. A new window will open.
        1. Under **Image files parameters**, click the … button and select the first file in the map sequence. Under End ind., enter the number for the last file in the sequence; the **Step** is generally set to 1. If this is true, the **# Points** should now be the total number of map pixels. Under **Save file parameters**, enter a file name.
        NOTE: The path can be ignored, as it is not read in the case of cluster calculations.
        2. Set up the NERSC parameters.
            1. Under **NERSC directory**, type in the user directory. This will be assigned when the user solicits cluster access from NERSC.
            2. Under **Image directory**, enter the file location on the cluster where the data are currently located.
            3. Under **Save directory**, enter the file location on the cluster where processed files will be saved.
            4. Under **Nb. of nodes**, enter how many nodes will be used for the calculation.
            NOTE: The total number of map points should be divisible by the number of nodes.
            5. Click on **create NERSC file** to generate the instruction file and save it. This file will be in a .dat format.

    2. Upload the .dat file to the NERSC cluster.
    NOTE: Typically, this is done with a data transfer program such as WinSCP.
    3. From a terminal window (logged into the NERSC account), run the executable file XMASparamsplit_new.exe. When prompted, type in the name of the NERSC .dat file.
    NOTE: The program will now execute, and nodes will be assigned to process each image file in sequence. Once a node completes its calculations, the data will be added to a sequence file called "sample name".seq. Copy the .seq file to the local machine.
    4. Open the .seq file.
        1. In XMAS, click on **Analysis | Read analysis sequential list**. This will open a new window.
        2. Load the .seq list by clicking on **load as struc** and selecting the .seq file from the local machine.
        3. Display the map by clicking on **Display**; this will open a new window. To select which column will correspond to the z values of the 2D z plot, select it from the drop-down menu.
        4. To export the data, click on **save as list** and save as a .txt or .dat file.
        NOTE: The contents of this file can then be uploaded into another plotting program if desired.

3. **Process the powder diffraction data.**
Note: There are several different types of analyses possible. These fall broadly into three different categories: integration of a full pattern over 2θ, mapping phase distribution using one representative peak for a particular phase, or mapping the preferred orientation of one peak.
    1. Integrate the entire pattern as a function of 2θ.
        1. Go to **Analysis | Integration along 2theta**. Select a 2θ range that covers the angles in the pattern, which can be found by hovering over any pixel of the pattern and reading the displayed 2θ value.
        2. Select a χ (azimuth) range.
        NOTE: Here, either the entire azimuthal range can be selected, or just certain regions, depending on the user preference.
        3. Click **Go to integrate**. Click **Save** to save the pattern.

    2. Map the phase locations by integrating one peak across 2θ and mapping it onto a 2D map.
        1. Select 2θ and χ ranges as in the previous step (but this time confined to only a subset of the entire pattern).
        NOTE: Usually only one peak, representative of a particular phase of interest, is selected. The ideal peak would not be expected to have any overlaps with other phases.
        2. Select a fit function (Gaussian or Lorentzian) and fit the peak by clicking the Go button. Make sure that the fit is good before proceeding.
        3. To map the phase location, go to **Automated Analysis | Set chi-twotheta analysis**; a new window will open. Select the path, start and end numbers, and a result file name, then click the arrow to start the scan.
        NOTE: The program will now map the previously fit peak on each pattern, and log the intensity, width, position, and d-spacing of the mapped peak onto the result file. The resulting file (usually a text file) can then be uploaded into any plotting program and plotted by the user.

    3. Map the preferred orientation by integrating one peak across χ and mapping it across a 2D map.
        1. Go to **Analysis | Integration along Chi**. A new window will open. As before, select 2θ and χ ranges that cover a peak displaying the preferred orientation.
        2. Select a fit function (Gaussian or Lorentzian) and fit by hitting the **Go** button.
        NOTE: The program will now divide χ into several bins, and will calculate the total intensity across each bin over the 2θ range specified. The result will be a plot of intensity as a function of χ. When fit, it will indicate the angular orientation of the highest intensity.
        3. To map across all files, go to **Automated Analysis | Set stage-chi analysis**. Select the path, start and end numbers, and a result file name, then click the arrow to start the scan.

NOTE: The program will map the same peak across all patterns, and generate a text file containing results as a function of motor position. These can then be plotted in any plotting program.

Representative Results

Laue Microdiffraction

A recent measurement and analysis was performed on a natural moissanite (SiC) sample[18]. The sample consisted of a piece of tuff embedded in an epoxy plug, which was then cut and polished to expose the ROI. Three moissanite grains were identified using optical microscopy and Raman spectroscopy (**Figure 1a**). One of the grains, SiC 2 (**Figure 1b**), was thought to contain native silicon (Si)[18]. The goal of the x-ray measurement was to identify the phase of silicon carbide and the crystallinity of silicon in the sample.

The sample was taped onto a glass slide using double-sided tape, and the slide was then attached to the conventional stage block. A silicon standard was placed beside it, which was used to calibrate the detector geometry as outlined in the procedure. The silicon standard consisted of an unstrained, lab-grown silicon single crystal cut to expose the (001) face. The sample and standard were placed on the stage at χ = 45° and the detector was positioned at 90° relative to the x-ray beam propagation direction.

The rough sample position was located using the camera alignment system on the beamline. The sample was then mapped using XRF (**Figure 1c**). Since silicon and carbon are too light to be detected by the XRF detector, the location of the crystal was determined based on a lack of XRF intensity, as the surrounding matrix is Ca- and Fe-rich. The XRF map was used to accurately determine the boundaries of the XRD map.

A 1,064 µm x 1,080 µm map was defined using 8 µm step size in both the x and y directions. A total of 17,955 Laue x-ray diffraction patterns were recorded using a 0.5 s exposure time. Indexing of moissanite was attempted with two of the most commonly found natural silicon carbide polytypes, 4H-SiC and 6H-SiC, using the XMAS software and the local XMAS computing cluster. Processing of the data set took under 20 min in this manner.

Both 4H-SiC and 6H-SiC are hexagonal (*P6₃mc*) crystal structures consisting of alternating Si and C layers along the *c* axis, with the main difference being the number of layers in each structure (4 versus 6) and therefore the length of the *c* axis (4H-SIC: a = 3.073 Å, c = 10.053 Å; 6H-SiC: a = 3.073 Å, c = 15.07 Å)[19]. Initial examination of the peak intensity (**Figure 2a**) clearly corresponds with both the microscopy and XRF image of the moissanite from **Figure 1**. Initial attempts at indexation were made using 4H-SiC as a starting model (**Figure 2b**). Manual analysis of a pattern from the body of the sample indicates that the 4H-SiC fitting is good (**Figure 2c**), and when mapping these results, it is clear that most of the crystal can easily be indexed as 4H-SiC (**Figure 2b**). The area to the bottom right, when manually examined, shows that the sample is polycrystalline, and is better indexed as 6h-SiC (**Figure 2d**).

When looking at a 6H-SiC indexing map (**Figure 3a**), one area stands out as having low indexing success. Upon closer examination, several overlapping diffraction patterns with broad and irregular diffraction peaks can be observed (**Figure 3b-d**). These index as silicon; at least three crystallites can be indexed, overlapping in the same region (**Figure 3**). Upon close examination of individual peaks, it can be seen that each grain consists of several subgrains, and that significant plastic deformation, demonstrated by the 3D peak shape (**Figure 3e-g**), is present in silicon.

Powder Microdiffraction

We measured a diffraction map of an olive snail shell (*Oliva fulgurator*, Grand Cayman Island) transect. The shell was mounted in an epoxy puck, which was then cut and roughly polished to expose the shell. The sample was then attached to the stage with double-sided tape and a stage rotation of χ = 15°, and a test pattern was recorded to determine the potential phase of interest (**Figure 4**). An XRF map was taken using Ca and Fe to locate the sample motor coordinates (**Figure 5a-b**).

For diffraction, the detector was placed at 50° with respect to the sample, and the beam monochromated to 8 keV (1.5498 Å). Powder diffraction patterns were taken over a 2,380 x 460 µm area in 20 µm steps using a 10 s exposure time. The 2,737 collected powder diffraction patterns clearly match that of aragonite throughout the entire measurement. The (040) width, d-spacing, and χ azimuthal angle of maximum intensity (as a qualitative measure of texture) were calculated for each pattern and plotted, showing a correlation between certain orientations and peak position/d-spacing (**Figure 5c-f**). The calculation is automated through XMAS, and this data set was processed on a desktop computer in under 1.5 h.

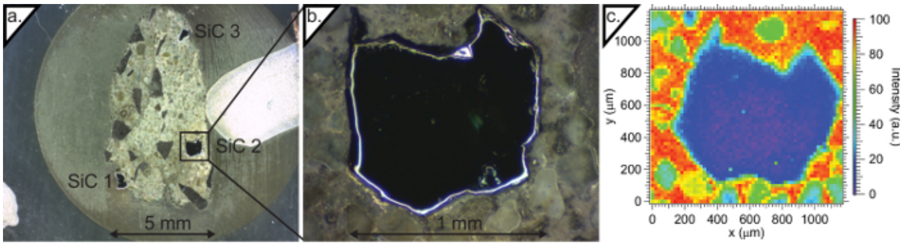

Figure 1. Moissanite sample (**a**) Moissanite sample embedded in epoxy puck. Three moissanite crystals can be optically identified. (**b**) Higher magnification microscope image of the region of interest. (**c**) X-ray fluorescence (XRF) map of the sample. The XRF measures all intensity from 2,000-20,000 eV. Since the Kα_1 emission lines of Si and C are 1,740 and 277 eV, respectively, the moissanite sample can be identified by a lack of measured intensity. Please click here to view a larger version of this figure.

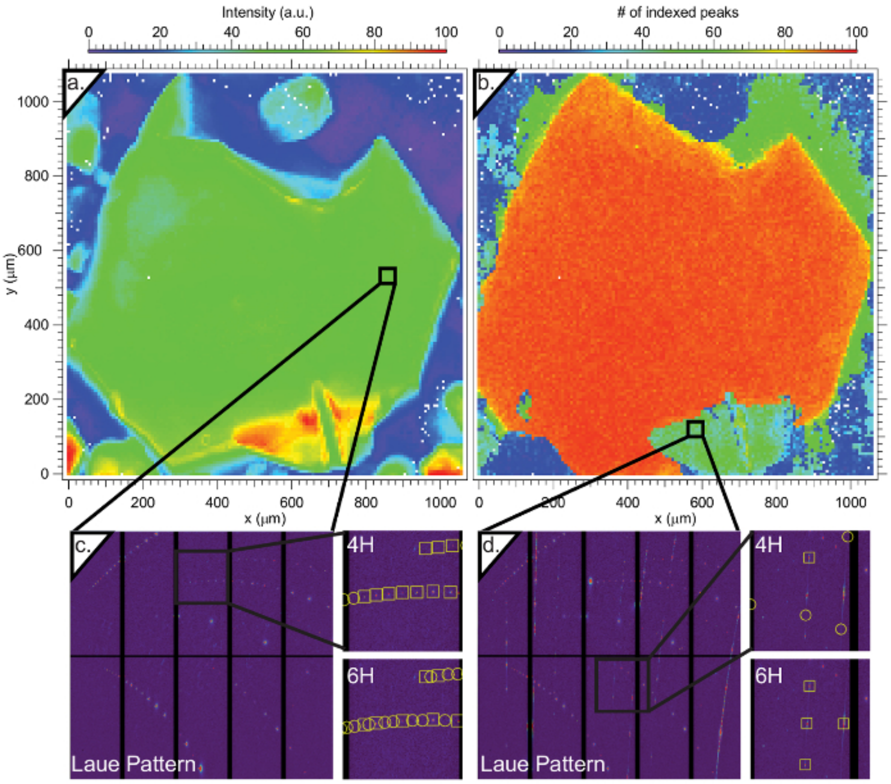

Figure 2. Single crystal indexing results for moissanite. (**a**) Average peak intensity over all measured patterns. The main outline of the moissanite can be easily seen. Other high-intensity regions correspond to other silicate or carbonate phases that are part of the surrounding host matrix. (**b**) Number of peaks indexed in the 4H-SiC phase. Discrepancies in sample shape between (a) and (b) are due to moissanite diffraction from below the exposed surface of the sample. (**c**) Indexing of a pattern from the main body of the crystal. Squares: peaks fit by the model. Circles: peaks expected by the model but not found in the diffraction pattern. The 4H-SiC provides a better fit, and fits all observed peaks with no additional peaks predicted. (**d**) Indexing of a pattern from the poorer-fit region of the sample. Here, 6H-SiC provides a better match. The 4H-SiC pattern from the single-crystal main body can also be seen, underlying the stronger 6H-SiC pattern. Please click here to view a larger version of this figure.

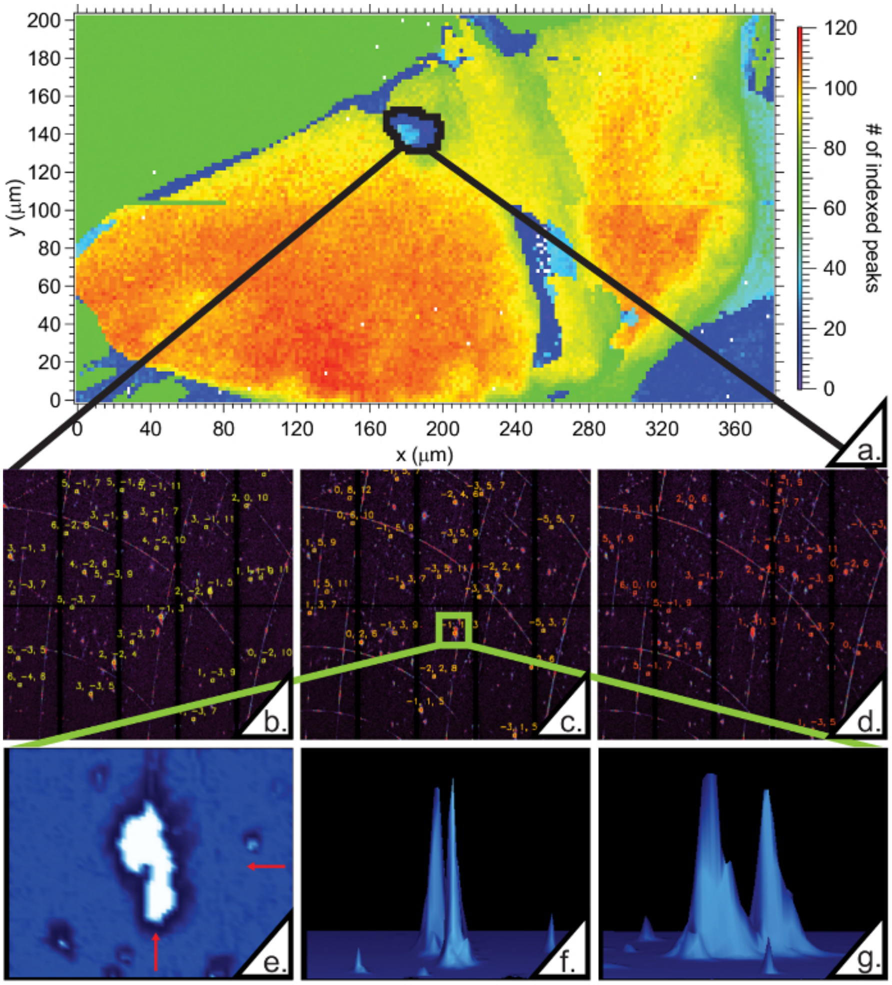

Figure 3. Indexing of plastically deformed multigrain Si. (**a**) Number of 6H-SiC peaks indexed by XMAS[17]. Area where silicon peaks are most intense, and silicon is exposed on the surface of the sample, is outlined in black. (**b-d**) Three Si grains can be observed within the area outlined in (a). (**e**) Detailed view of pattern, containing the (-113) peak of grain (c) and the (1-13) peak of grain (d). Arrows indicate the direction of view for: (f), vertical; (g), horizontal. At the magnification present in (f) and (g) (signal to noise = 25), it can be seen that there are several other local maxima at the bases of these two peaks, which indicate the formation of subgrains due to plastic deformation of silicon in this sample. Please click here to view a larger version of this figure.

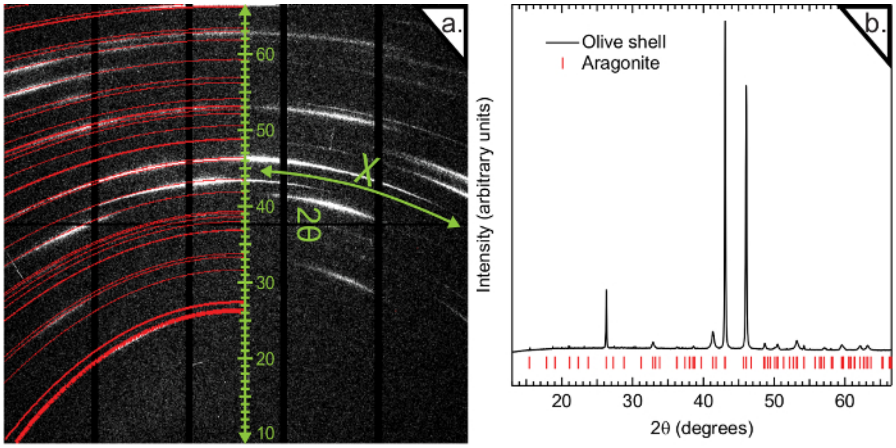

Figure 4. Aragonite patterns in olive snail shell. (**a**) Raw olive snail shell pattern, with aragonite pattern (red) overlayed. The 2θ and χ integration directions are indicated. (**b**) 1D integrated olive snail shell pattern. λ = 1.54982. Please click here to view a larger version of this figure.

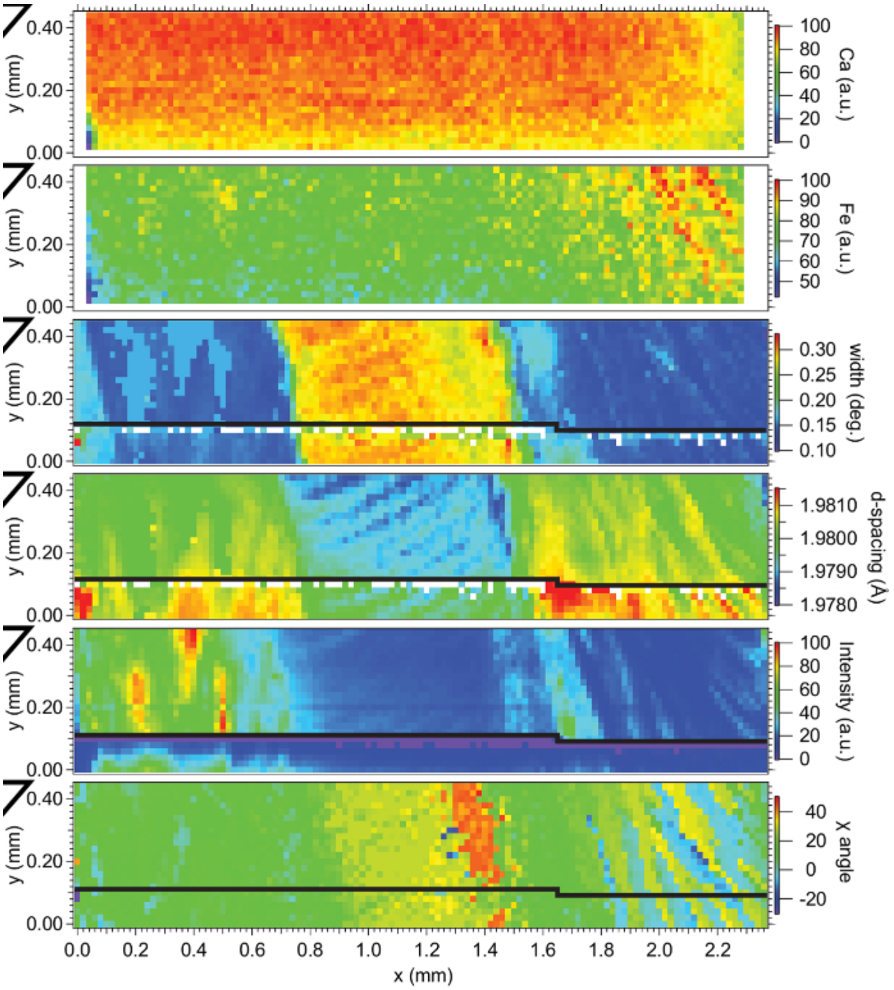

Figure 5. Olive snail shell map. Normalized x-ray fluorescence (XRF) of (**a**) Ca and (**b**) Fe. Aragonite (040) peak (**c**) width, (**d**) d-spacing, (**e**) integrated intensity, and (**f**) χ angle. White pixels correspond to missing pixels. Black bar corresponds to location in the map above which the M201 mirror was retuned. Please click here to view a larger version of this figure.

Discussion

We present a method for combined x-ray diffraction and XRF analysis of crystalline samples at ALS beamline 12.3.2. While neither Laue diffraction, powder diffraction, nor XRF themselves are novel methods, beamline 12.3.2 combines them as well as a micron-scale x-ray beam size, a scanning stage system that is correlated to detector exposure triggers, and a comprehensive analysis software to allow for experiments that would not be possible on laboratory instruments. Photon flux at the beamline is several orders of magnitude higher than what is achievable on laboratory instruments. Additionally, typical Laue diffraction laboratory instruments are designed only for orientation determination on single crystals, but are incapable of mapping on any scale, while laboratory powder diffractometers are only designed for bulk measurements, and beam sizes often exceed several hundreds of microns in dimension. Another major benefit of this beamline, which was not addressed in the protocol, is that *in situ* experiments can and are routinely performed. The beamline has heating and cooling capabilities, and the large working distance of the instrument relative to the typical sample size allows users to also bring in their own stages, such as a diamond anvil cell, and perform either Laue or powder diffraction in this manner[6].

Combined XRF/Laue measurements are comparable to SEM measurements using E/WDS and EBSD. These techniques are commonly employed in geoscience, and can be used for phase identification and determining angular resolution[20]. However, beamline 12.3.2 has several advantages over SEM with E/WDS and EBSD. The data in the procedure described here can be collected at standard temperature and pressure, so no special preparation must be made for samples to be placed in a vacuum system, as is required with an SEM. EBSD is very sensitive to the surface of the sample, and so requires much greater care in polishing in order not to destroy the surface crystal lattice. In contrast, Laue diffraction is somewhat of a bulk method; the x-ray beam penetration can reach as much as 100 µm, although most of the diffracted signal will come from the top ~10 µm. If a conductive coat has already been applied, sample diffraction can still be easily seen in the case of Laue diffraction (as the coating is polycrystalline and will not generate a coherent signal in white beam mode), but may be difficult in the case of EBSD. Also, EBSD may not be possible for samples which have experienced severe plastic deformation, but Laue diffraction is routinely performed on such samples (**Figure 3**). Both methods are fast; for a well-crystallized sample, up to 10,000 Laue patterns can be collected per hour. However, downsides to using Laue include restrictions on the amount of synchrotron time versus that of a laboratory SEM, potentially higher costs (while synchrotron time is free to users, physical access may require some travel costs which are not covered by the synchrotron facility), the difficulty of performing quantitative elemental determination (which is common on laboratory E/WDS systems), and finally, SEM software may be more user friendly than XMAS, as the software development teams are generally much larger for commercial software products.

Several steps within the technique are critical. Proper calibration is crucial if accurate strain or d-spacing results are necessary. The focal point is determined by measuring the incident beam width at different focal distances prior to any other experiments being performed and independently of the calibration procedure. When performing the calibration, the sample must be raised to the same height (z) as the calibrant (the calibrants used are either synthetic silicon, synthetic quartz, yttrium aluminum garnet, or alumina powder, depending on the type of experiment being performed). However, in the case of samples placed at a shallow or glancing angle, a small displacement in the Z direction can lead to a fairly large displacement in Y, and consequently to a significant shift in the position of the diffracting sample relative to the focal point of the beam. In cases where positional errors have been observed, we find that an average over a sample map can function as a reasonable sample-to-detector calibrant, with mapped strains then being relative to the average rather than an outside calibrant. This sample geometry is less common in geophysical applications, confined mostly to when large (> 4 Å) d-spacings must be measured in a reflective geometry using monochromatic light. When performing the calibration, the sample is assumed to be unstrained, so any deviations from the calibrant peaks' angular relationships in the indexation and strain calculation are assumed to come from deviations in the "known" detector position with respect to the sample. When sample strain is calculated, the detector parameters are assumed to be well known, so any deviations will be treated as being a result of deviatoric strain in the sample. Consequently, the two types of refinement are highly correlated, and only one type must be used at a time.

Care must also be taken when processing data. Details of the mathematical processes behind XMAS can be found in Tamura[17]. When indexation and strain refinement are each performed, the program opens a separate window with a large volume of information, such as peak hkl, peak energy, intensity, the orientation of the crystal, deviatoric strain parameters, *etc.* If the correct stiffness tensor was used, the program will also use the stress-strain relationship to calculate a variety of stress tensors and values, which will also be displayed, in units of MPa. When automating these processes, three different methods exist. While the NERSC method is presented here, automation can also proceed on a local machine or on a local cluster. In all cases, the output will be a .seq file, containing much of the same information as in the individual indexation and strain refinement output windows, but tabulated so that each row corresponds to one diffracted pixel. In general, the automation program relies on good initial guesses to ensure good results. For example, in the case of moissanite (**Figure 2b**), pixels in the 6H-SiC region could be indexed as 4H-SiC with a large number of coincident peaks (40+). When looking at the map of indexed peaks (**Figure 2b**), it is clear that the 6H-SiC region is not being indexed correctly from the simple fact that the correctly indexed region fits more than 70 peaks per pixel. When indexed as 4H-SiC, it can be seen that not all peaks are fit (**Figure 2d**), which indicates that the crystal structure is a misfit. When the misfit area of the sample is manually examined, it becomes clear that the sample is polycrystalline. The 4H-SiC crystal peaks can be visually identified and are in broadly the same positions on the detector image as in **Figure 2c**. Another, stronger intensity, pattern lies on top. This pattern can be indexed as 6H-SiC (**Figure 2d**). The contrast between these two regions within the sample and their closely related unit cells serves to show that care must be taken when indexing; even if a high number of peaks is indexed (as in the case where 4H-SiC is incorrectly mapped to ~40 peaks), the model may still be wrong, and manual verification is needed. The proportion of non-indexed reflections and/or of missing reflections (predicted but not found) provides good indication of misindexation. However, manual verification was required to determine whether this area was subject to a different orientation (which may have a different number of visible peaks), was plastically deformed or nanocrystalline (which may lead to trouble in the peak finding protocol), or was misindexed as is the case here. This example demonstrates that initial automated mapping results may require additional verification before conclusions can be drawn about the sample.

Figure 5 also shows a number of important issues that may arise. For example, the Fe XRF signal appears at first to correlate with the orientation and d-spacing plots, which suggests that those variations are due to compositional variation. However, when verified using SEM/energy-dispersive spectroscopy (courtesy of the Kai Chen group at Xi'an Jiaotong University, Xi'an, China), the compositional variation was not observed. This demonstrates that unusual or unexpected signal variations in XRF must be manually verified. In this case, we re-measured individual XRF spectra and determined that the increase in intensity was due to the differently oriented layers of the shell, which functioned as a diffraction grating that somewhat coincided with the Fe signal. The reason this measurement error occurred is broadly twofold. The first reason is that the XRF signal was induced using a polychromatic (white) beam, which has an increased likelihood that an elastic signal (from diffraction, such as may be caused by a diffraction grating) is picked up by the detector. The second reason lies with the manner in which XRF data are acquired: when a XRF map is automated, the raw spectra are not saved for each pixel. Rather, the total counts over a particular spectral range are tabulated for each pixel and saved in a .txt output file. In the case of this particular map, the Fe signal actually measures total intensity between 6,200-7,316 eV, so a grating that diffracts any energy within that range such that it is aimed at the XRF detector would cause a spike in perceived Fe concentration. This brings up another potential misstep: the elemental range must be carefully considered and chosen prior to the beginning of the measurement, in such a way that the chosen peaks do not overlap with other potential elements that the sample may contain. Additionally, manual verification of the XRF spectrum at particular pixels allows users to observe whether the spectra look reasonable for particular elements. Alternatively, a monochromatic fluorescence scan may not generate the diffraction peak that caused this spike, but monochromatic scans are much slower due to lower flux.

In **Figure 5c-d**, one or two rows of mostly-missing pixels can be observed; these data points were collected but the peak fitting program failed for these particular patterns. In this case, XMAS struggled with the integration protocol because the x-ray beam had drifted throughout the long measurement, leading to a drop in the photon flux. This was corrected manually during the data collection, after which the peak intensity increased dramatically (**Figure 5e**). It is important that the beam be monitored throughout the data collection process, to ensure that the signal to noise ratio is large enough for the data to be processed. The data collection software has the ability to automatically stop or restart the collection if the IC counts dip below a user-determined threshold.

Future development will focus on decreasing beam size, decreasing collection time, increasing beam stability, and optical system improvements for better sample visualization during data collection. We are also working on developing a new platform of independent and improved software for data analysis that is not dependent on user access to a third party software (*e.g.*, XMAS currently requires the use of a runtime version of IDL for its data visualization interface).

Disclosures

The authors have nothing to disclose.

Acknowledgements

This research used resources of the Advanced Light Source, which is a DOE Office of Science User Facility under contract no. DE-AC02-05CH11231. We would also like to acknowledge Drs. L. Dobrzhinetskaya and E. O'Bannon for contributing the moissanite sample, C. Stewart for her olive snail shell data, H. Shen for preparing the olive snail shell, and G. Zhou and Prof. K. Chen for EDS measurements on the olive snail shell.

References

1. Li, Y. *et al.* A synchrotron study of defect and strain inhomogeneity in laser-assisted three-dimensionally-printed Ni-based superalloy. *Applied Physics Letters.* **107** (18), 181902 (2015).
2. Zhou, G. *et al.* Real-time microstructure imaging by Laue microdiffraction: A sample application in laser 3D printed Ni-based superalloys. *Scientific Reports.* **6**, 28144 (2016).
3. Tippabhotla, S.K. *et al.* Synchrotron X-ray Micro-diffraction - Probing Stress State in Encapsulated Thin Silicon Solar Cells. *Procedia Engineering.* **139**, 123-133 (2016).
4. Xu, C.-Z. *et al.* Elemental Topological Dirac Semimetal: α-Sn on InSb(111). *Phys Rev Lett.* **118** (14), 146402 (2017).
5. Chen, X., Tamura, N., MacDowell, A., James, R.D. In-situ characterization of highly reversible phase transformation by synchrotron X-ray Laue microdiffraction. *Appl Phys Lett.* **108** (21), 211902 (2016).
6. Zhou, X. *et al.* Reversal in the Size Dependence of Grain Rotation. *Phys Rev Lett.* **118** (9), 096101 (2017).
7. Stan, C.V., Beavers, C.M., Kunz, M., Tamura, N. X-Ray Diffraction under Extreme Conditions at the Advanced Light Source. *Quantum Beam Science.* **2** (1), 4 (2018).
8. Chen, K., Kunz, M., Tamura, N., Wenk, H.-R. Residual stress preserved in quartz from the San Andreas Fault Observatory at Depth. *Geology.* **43** (3), 219-222 (2015).
9. Chen, K., Kunz, M., Tamura, N., Wenk, H.-R. Evidence for high stress in quartz from the impact site of Vredefort, South Africa. *Eur J Mineral.* **23** (2), 169-178 (2011).
10. Jackson, M.D. *et al.* Material and Elastic Properties of Al-Tobermorite in Ancient Roman Seawater Concrete. *J Am Ceram Soc.* **96** (8), 2598-2606 (2013).
11. Jackson, M.D. *et al.* Phillipsite and Al-tobermorite mineral cements produced through low-temperature water-rock reactions in Roman marine concrete. *Am Mineral.* **102** (7), 1435-1450 (2017).
12. Gilbert, P.U.P.A. *et al.* Nacre tablet thickness records formation temperature in modern and fossil shells. *Earth Planet Sc Lett.* **460**, 281-292 (2017).
13. Mass, T. *et al.* Amorphous calcium carbonate particles form coral skeletons. *P Natl Acad Sci.* **114** (37), E7670-E7678 (2017).
14. Marcus, M.A. *et al.* Parrotfish Teeth: Stiff Biominerals Whose Microstructure Makes Them Tough and Abrasion-Resistant To Bite Stony Corals. *ACS Nano.* **11** (12), 11856-11865 (2017).
15. Kunz, M. *et al.* A dedicated superbend x-ray microdiffraction beamline for materials, geo-, and environmental sciences at the advanced light source. *Rev Sci Instrum.* **80** (3), 035108 (2009).
16. Beckhoff, B., Kanngießer, B., Langhoff, N., Wedell, R., Wolff, H. *Handbook of Practical X-Ray Fluorescence Analysis.* Springer Science & Business Media. (2007).
17. Tamura, N. XMAS: A Versatile Tool for Analyzing Synchrotron X-ray Microdiffraction Data. *Strain and Dislocation Gradients from Diffraction.* 125-155 (2014).
18. Dobrzhinetskaya, L. *et al.* Moissanite (SiC) with metal-silicide and silicon inclusions from tuff of Israel: Raman spectroscopy and electron microscope studies. *Lithos.* (2017).
19. Thibault, N.W. Morphological and structural crystallography and optical properties of silicon carbide (SiC): Part II: Structural crystallography and optical properties. *American Mineralogist.* **29** (9-10), 327-362 (1944).
20. *Electron Backscatter Diffraction in Materials Science.* at <//www.springer.com/us/book/9780387881355>. Springer US. (2009).